International Journal of Mechanical Sciences 270 (2024) 109063

Contents lists available at ScienceDirect

International Journal of Mechanical Sciences

journal homepage: www.elsevier.com/locate/ijmecsci

Explicit boundary thickening direct forcing immersed boundary method

Buchen Wu [a,b,e], HsuChew Lee [b], Chang Shu [a,*], Minping Wan [b,c,d,*]

[a] Department of Mechanical Engineering, National University of Singapore, 10 Kent Ridge Crescent, Singapore, 119260, Singapore
[b] Guangdong Provincial Key Laboratory of Turbulence Research and Applications, Department of Mechanics and Aerospace Engineering, Southern University of Science and Technology, Shenzhen, 518055, Guangdong, China
[c] Guangdong-Hong Kong-Macao Joint Laboratory for Data-Driven Fluid Mechanics and Engineering Applications, Southern University of Science and Technology, Shenzhen, 518055, Guangdong, China
[d] Jiaxing Research Institute, Southern University of Science and Technology, Jiaxing, 314031, Zhejiang, China
[e] Department of Mechanical and Aerospace Engineering, The Hong Kong University of Science and Technology, Clear Water Bay, Kowloon, Hong Kong

ARTICLE INFO

Keywords:
Immersed boundary method
Implicit direct forcing
Boundary thickening direct forcing
Second-order approximation

ABSTRACT

For simulating the fluid–structure interaction (FSI) problems with moving boundaries and large deformations, the original implicit direct forcing (IDF) immersed boundary method (IBM) has to construct and inverse a large correlation matrix which contains the local relationships between the Lagrangian points and their surrounding Eulerian points. Consequently, as the number of Lagrangian points increases, the IBM procedure experiences exponential growth in both memory consumption and computational time. In this work, we first proposed an implicit boundary thickening direct forcing (BTDF) scheme that combines the correlation between the thicknesses of the solid and fluid forcing shells with the IDF scheme. By employing Taylor series expansion, a second-order approximation is derived through error analysis, which allows the force density to be explicitly calculated with second-order accuracy without the construction and inversion of the correlation matrix. With this second-order approximation, we proposed an explicit BTDF scheme to achieve high computational efficiency and maintain similar accuracy as the implicit BTDF scheme. The comparisons of the memory consumption and computational cost between the explicit and implicit BTDF-IBs demonstrate that the explicit BTDF scheme is not only computational efficient, but also has memory saving performance. The proposed explicit and implicit BDTF-IBs integrated with the reconstructed lattice Boltzmann flux solver (RLBFS) (Lu et al., 2022) are validated by the numerical simulations of flow past an in-line oscillating cylinder, particle sedimentation, and flow past a 3D flexible plate. The results show that both the explicit and implicit BTDF-IBs provide almost identical solutions, and the instantaneous boundary velocity errors in the explicit BTDF scheme maintain the second-order accuracy.

1. Introduction

Fluid–structure interaction (FSI) problems have gained increased focus due to their extensive application across scientific research and engineering [1–5]. The immersed boundary method (IBM) has been widely utilized to solve challengeable FSI problems involving moving boundaries and large deformations [6–17], such as bionic fish swimming [18–23], bionic bird/insect flight [24–26], and transport of cells [27–29], owing to its simple yet robust methodology for simulating complex FSI problems. In contrary to conventional numerical approaches with body-fitted grids, such as the finite element method [30–32] and arbitrary–Lagrangian–Eulerian (ALE) method [33–37], IBM circumvents the tedious grid regeneration process and saves amount of considerable computational time. The concept of IBM is firstly proposed by Peskin [38], where the IBM is adopted to simulate the dynamic interactions between the blood flow and the heart leaflets.

The original IBM proposed by Peskin [38] belongs to the penalty forcing IBM, where Hooke's law is employed to model the restoring force with user-defined artificial stiffness. Many variants of IBMs have been developed to model the restoration force accurately. Goldstein et al. [39] introduced the control theory into the IBM framework and developed a feedback forcing scheme to evaluate the restoration force. Subsequently, Mohd-Yusof [40] and Fadlun et al. [41] proposed a direct forcing scheme based on the difference between the desired velocity and the unforced fluid velocity at the Lagrangian points. This approach eliminates the need for user-specified parameters in the penalty forcing scheme. However, complex point identification algorithms and complicated interpolation approaches are required to

---

* Corresponding authors.
E-mail addresses: mpeshuc@nus.edu.sg (C. Shu), wanmp@sustech.edu.cn (M. Wan).

https://doi.org/10.1016/j.ijmecsci.2024.109063
Received 5 November 2023; Received in revised form 23 January 2024; Accepted 23 January 2024

reconstruct the velocity and pressure fields around the IB interface in the original direct forcing scheme. Later, the direct forcing scheme is further improved with the regularized delta function by Uhlmann [42], which greatly enhances the computational efficiency and suppresses the numerical oscillation. The IBM with direct forcing scheme has since become a popular numerical approach for simulating FSI problems [43–45], thanks to its straightforward implementation and effectiveness in reducing spurious oscillations. However, due to the explicit approach used in the IB forcing step, the original one-step direct forcing scheme is unable to accurately model the mutual interaction between the flow field and the immersed object. Consequently, the no-slip boundary condition may not be reliably enforced on the solid boundary. Su et al. [46] proposed an improved direct forcing scheme which utilizes a banded matrix that incorporates the data of the Lagrangian–Eulerian field. While this improved direct forcing scheme resulted in significantly lower boundary velocity errors when compared to the original direct forcing scheme, the no-slip boundary condition may not be fully satisfied due to the explicit procedure employed in the momentum equations. To reduce the boundary velocity errors, the multi-direct forcing (MDF) scheme [47–50] is proposed to satisfy the no-slip boundary condition through multiple forcing iteration steps. Owing to the simple and straightforward nature of the multi-direct forcing scheme, it has been widely utilized to solve a wide-range of FSI problems [51–54]. However, the improved accuracy of the multi-direct forcing scheme comes at the cost of requiring much more computational effort when simulating FSI problems involving multiple objects and moving boundaries.

Kempe and Fröhlich [50] proposed the implicit direct forcing (IDF) scheme to consider the mutual interaction between the flow field and the solid object by taking into consideration of the inequality between the interpolation and the spreading operation. Subsequently, Jiang and Liu [55] extended the implicit direct forcing scheme to the lattice Boltzmann method (LBM) framework, where they also systematically investigated the correlation between the thickness of solid forcing shell and the regularized delta functions. Although the implicit direct forcing scheme can achieve highest accuracy among all variants of direct forcing schemes, it has to construct a correlation square matrix and inverse it at each time step for FSI problems with moving boundaries. Therefore, the memory requirement and computational time would grow exponentially with the number of Lagrangian points. It may explain the reason that although the implicit direct forcing scheme has been proposed, Kempe and Fröhlich [50] did not implement the IDF scheme in their work. Park et al. [56] circumvented the direct inversion of large correlation matrix in the implicit direct forcing scheme by introducing Taylor series expansion on the correlation matrix, yielding a recurrence equation for the iterative forcing step. Subsequently, Xu and Choi [57] extended this direct forcing scheme to simulate FSI problems in thermal flows. While the direct inversion is eliminated, the recurrence equation for the iterative forcing involves a complex iterative procedure. Based on the correlation between the solid forcing shell's thickness and the regularized delta functions, Jiang and Liu [55] proposed a boundary thickening direct forcing (BTDF) scheme by increasing slightly the thickness of the solid forcing shell in the framework of the multi-direct forcing scheme. They claimed that the BTDF can achieve similar accuracy as the implicit direct forcing scheme with a much lower computational cost. However, certain issues in the original BTDF remain unresolved, including the unknown convergence rate, the optimal iteration number, and the accuracy order of the boundary velocity errors.

In this work, to achieve high computational efficiency and maintain similar accuracy as the original IDF scheme, we propose an explicit variant of the IDF scheme. We first develop the implicit BTDF scheme by combining the correlation between the thickness of the solid forcing shell and the delta function with the IDF scheme. Using the Taylor series expansion, we can obtain a second-order approximation through error analysis. This second-order approximation allows the linear equation system in the implicit BTDF scheme to be explicitly resolved without constructing and inversing the large correlation matrix; thus, the force density at Lagrangian points can be predicted with second-order accuracy. Based on this approximation, we propose an explicit BTDF scheme that maintains similar accuracy as the implicit BTDF scheme but achieves high computational efficiency.

The paper is organized as follows: the governing equations, the numerical method for fluid dynamics, and the original implicit boundary thickening direct forcing immersed boundary method are introduced in Section 2. In Section 3.1, the detailed derivation of the second-order approximation is performed. Subsequently, the comparisons of the memory consumption and computational time between the explicit and implicit BTDF-IBs are presented in Section 3.2. In Section 4, the numerical accuracy test and numerical validations of the proposed explicit BTDF-IB are conducted. Conclusions are provided in Section 5.

2. The mathematical model and numerical approach

In this section, the governing equations for modeling fluid–structure interaction problems are introduced, where the fractional step method is employed to decouple the solution procedure of the Navier–Stokes equations into the prediction and forcing steps. In the prediction step, the reconstructed lattice-Boltzmann flux solver (RLBFS) [58] is applied to calculate the flow variables. Subsequently, IBM is introduced to correct the predicted flow field, ensuring that the no-slip boundary condition is accurately satisfied on the immersed interface. Note that the original implicit direct force IBM with boundary thickening technique is presented in this section.

2.1. Navier–Stokes (N-S) equations

Based on the mass and momentum conservation laws for incompressible flows, the macroscopic governing equations can be written in a weakly compressible form as:

$$\frac{\partial \rho}{\partial t} + \nabla \cdot (\rho \mathbf{u}) = 0, \tag{1a}$$

$$\frac{\partial (\rho \mathbf{u})}{\partial t} + \nabla \cdot (\rho \mathbf{u}\mathbf{u}) = -\nabla p + \nu \nabla \cdot \left[\nabla \rho \mathbf{u} + (\nabla \rho \mathbf{u})^T \right] + \mathbf{f}, \tag{1b}$$

where ρ denotes the density of fluid, $\mathbf{u}$ is the flow velocity, ν is the kinematic viscosity, p is the pressure, and $\mathbf{f}$ is the volume force density term. If the density variation is small and Mach number is low, the above N-S equations can be applied to simulate incompressible flows.

Briefly, the solution of the Navier–Stokes equations is split into two steps, namely, the prediction and forcing steps. In the prediction step, the volume forcing density term is excluded from the governing equations. The N-S equations are discretized by the finite volume method to predict the density at next time step ρ^{n+1} and the intermediate flow velocity $\mathbf{u}^*$, where RLBFS [58] is employed to evaluate the viscous and inviscid fluxes on the cell interface. Subsequently, in the forcing step, the IBM is utilized to spread the force density at Lagrangian points to the surrounding Eulerian points; thereby, the intermediate flow field can be corrected to satisfy the no-slip boundary condition. The equations are solved as follow:

$$\frac{\partial \mathbf{W}}{\partial t} + \nabla \cdot \mathbf{F} = 0, \quad \text{prediction step} \tag{2a}$$

$$\frac{\partial (\rho \mathbf{u})}{\partial t} = \mathbf{f}, \quad \text{forcing step} \tag{2b}$$

where

$$\mathbf{W} = \left\{ \begin{array}{c} \rho \\ \rho \mathbf{u} \end{array} \right\}, \quad \mathbf{F} = \left\{ \begin{array}{c} \rho \mathbf{u} \\ \rho \mathbf{u}\mathbf{u} + p\boldsymbol{I} - \nu \left(\nabla \rho \mathbf{u} + (\nabla \rho \mathbf{u})^T \right) \end{array} \right\}. \tag{3a}$$

Since the flow solver has been developed in our previous work, readers are referred to [58] for detailed information on the RLBFS solver.

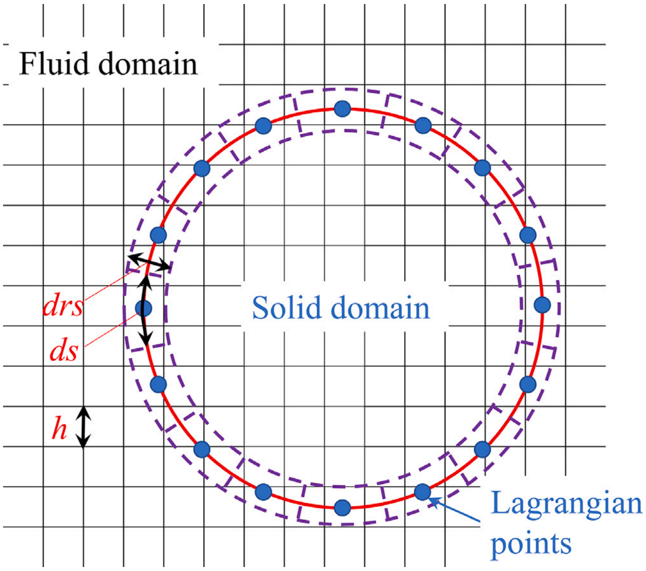

Fig. 1. Illustration of the boundary thickening direct forcing immersed boundary method around the solid surface, where h, ds and drs denote the Eulerian grid spacing, the Lagrangian point step, and the thickness of the solid forcing shell, respectively. The red circle line is the interface of the solid object, and the circle band ring formed by the two purple dashed circle lines denotes the solid forcing shell. In this work, $drs = 1.9h$ is adopted in the boundary thickening direct forcing immersed boundary method.

2.2. *Implicit boundary thickening direct forcing IBM*

In this subsection, the methodology of the proposed implicit boundary thickening direct forcing immersed boundary method is introduced. The implicit BTDF is a combination of the implicit direct forcing scheme and the correlation between the thicknesses of the solid and fluid forcing shells. For simplicity, the methodology is presented here for 2D problems. The solid forcing shell (represented by the two purple dashed circles) shown in Fig. 1 is crucial for the Lagrangian force density spreading. Jiang and Liu [55] demonstrated that it is essential to derive a proper relationship between the solid forcing shell and the fluid forcing shell (which depends on the discrete delta function) to accurately satisfy the no-slip boundary condition. Following the suggestion of Jiang and Liu [55], we employed a 3-point delta function with a solid forcing shell's thickness of $drs = 1.9h$ in this present work.

In the forcing step, Eq. (2b) can be discretized as:

$$\mathbf{f} = \rho \frac{\left(\mathbf{u}^{n+1} - \mathbf{u}^{*}\right)}{\Delta t}. \tag{4}$$

Assume that there are N_E Eulerian points around the Lagrangian point $\boldsymbol{X}_B^i$, the velocity at a Lagrangian point can be interpolated by

$$\begin{gathered}\boldsymbol{U}_B\left(\boldsymbol{X}_B^i\right) = \sum_j \mathbf{u}\left(\boldsymbol{r}_j\right) \cdot D_I\left(\boldsymbol{r}_j - \boldsymbol{X}_B^i\right), \\ i = 1, 2, \ldots, N_L, \quad j = 1, 2, \ldots, N_E,\end{gathered} \tag{5}$$

where $\boldsymbol{U}_B$ denotes the local boundary velocity at Lagrangian points. N_L and N_E represent the numbers of Lagrangian points and Eulerian points, respectively. D_I denotes the interpolation matrix with a dimension of $N_L \times N_E$ and it is given as:

$$D_I\left(\boldsymbol{r}_j - \boldsymbol{X}_B^i\right) = \frac{1}{h^2}\delta\left(\frac{r_j^x - X_B^i}{h}\right)\delta\left(\frac{r_j^y - Y_B^i}{h}\right) \cdot h^2. \tag{6}$$

Similarly, the Lagrangian force density spreading can be expressed as:

$$\begin{gathered}\mathbf{f}\left(\boldsymbol{r}_j\right) = \sum_i \mathbf{F}_B^i\left(\boldsymbol{X}_B^i\right) \cdot D_E\left(\boldsymbol{r}_j - \boldsymbol{X}_B^i\right) \cdot ds^i, \\ i = 1, 2, \ldots, N_L, \quad j = 1, 2, \ldots, N_E,\end{gathered} \tag{7}$$

where $\mathbf{F}_B$ is the lagrangian force density and D_E denotes the spreading matrix with a dimension of $N_E \times N_L$ as follows:

$$D_E\left(\boldsymbol{r}_j - \boldsymbol{X}_B^i\right) = \frac{1}{h^2}\delta\left(\frac{r_j^x - X_B^i}{h}\right)\delta\left(\frac{r_j^y - Y_B^i}{h}\right) \cdot drs. \tag{8}$$

The 3-point delta function is adopted in this present work to achieve a good balance between numerical efficiency and smoothing properties [59], and it is given as follows:

$$\delta(r) = \begin{cases} \left[1 + \sqrt{1 - 3(r)^2}\right]/3, & |r| \le 0.5, \\ \left[5 - 3|r| - \sqrt{1 - 3(1 - |r|)^2}\right]/6, & 0.5 < |r| \le 1.5, \\ 0, & |r| > 1.5. \end{cases} \tag{9}$$

Substituting Eq. (7) into Eq. (4) and then into Eq. (5) yields the following equation:

$$\begin{aligned} &\sum_j D_I\left(\boldsymbol{r}_j - \boldsymbol{X}_B^k\right) \cdot \left(\sum_i \mathbf{F}_B^i\left(\boldsymbol{X}_B^i\right) \cdot D_E\left(\boldsymbol{r}_j - \boldsymbol{X}_B^i\right) \cdot ds^i\right) \\ &= \frac{\rho}{\Delta t}\left(\sum_j \mathbf{u}^{n+1}\left(\boldsymbol{r}_j\right) \cdot D_I\left(\boldsymbol{r}_j - \boldsymbol{X}_B^k\right) - \sum_j \mathbf{u}^{*}\left(\boldsymbol{r}_j\right) \cdot D_I\left(\boldsymbol{r}_j - \boldsymbol{X}_B^k\right)\right) \\ &= \frac{\rho}{\Delta t}\left(\boldsymbol{U}_B\left(\boldsymbol{X}_B^k\right) - \sum_j \mathbf{u}^{*}\left(\boldsymbol{r}_j\right) \cdot D_I\left(\boldsymbol{r}_j - \boldsymbol{X}_B^k\right)\right). \end{aligned} \tag{10}$$

Therefore, the above equation can be rewritten in matrix form:

$$\left(D_I D_E\right)\mathbf{F}_B ds = \frac{\rho}{\Delta t}\left(\boldsymbol{U}_B - D_I \mathbf{u}^{*}\right), \tag{11}$$

The hydrodynamic force exerted on the moving immersed object can be evaluated with the force density as:

$$\mathbf{F}_f = -\sum_{i=1}^{N_L} \mathbf{F}_B^i ds^i \cdot drs + \rho V_s \frac{\Delta \boldsymbol{U}_s}{\Delta t} = -\sum_{j=1}^{N_E} \mathbf{f}^j \cdot h^2 + \rho V_s \frac{\Delta \boldsymbol{U}_s}{\Delta t}, \tag{12}$$

where V_s and U_s represent the volume and mass center's velocity of the immersed object, respectively.

The procedure of the original implicit BTDF-IB is summarized in **Algorithm 1**. The implicit BTDF-IB algorithm requires a significant amount of memory and time to construct the correlation matrix $D_I D_E$ and its inverse $(D_I D_E)^{-1}$ when dealing with a large number of Lagrangian points. In this work, the Gaussian elimination method is employed to compute the matrix inversion.

3. Explicit boundary thickening direct forcing IBM

In this section, a second order approximation of the implicit BTDF is derived through the error analysis based on the Taylor series expansion. Subsequently, the requirement of constructing large correlation matrix and its inversion in the implicit BTDF scheme is eliminated through the aid of second order approximation. Therefore, the explicit BTDF-IB is proposed in this study to efficiently solve FSI problems with a large number of Lagrangian points. Subsequently, the comparisons of the memory consumption and computational time between the implicit and explicit BTDF schemes are conducted to highlight the superiority of the proposed explicit BTDF scheme.

3.1. *Derivation of the second order approximation*

In this subsection, the details on the derivation of the second order approximation are presented. Eq. (11) can be rewritten as:

$$\sum_{i=1}^{N_L}(D_I^k D_E^i)\mathbf{F}_B^i ds^i = \frac{\rho}{\Delta t}\left(\boldsymbol{U}_B^k - D_I^k \mathbf{u}^{*}\right). \tag{13}$$

It can be seen that the correlation between the Lagrangian force density $\mathbf{F}_B$ and the RHS terms exists only when $D_I^k D_E^i \ne 0$. Thus, the above equation can be rewritten as:

$$\sum_{i \in D_I^k D_E^i \ne 0}(D_I^k D_E^i)\mathbf{F}_B^i ds^i = \frac{\rho}{\Delta t}\left(\boldsymbol{U}_B^k - D_I^k \mathbf{u}^{*}\right), \tag{14}$$

Algorithm 1 The original implicit BTDF-IB

```
Step 1: $\boldsymbol{D_I}$ and $\boldsymbol{D_E}$
Step 2: Construct the matrix $\boldsymbol{D_I D_E}$
Step 3: Solve the inverse matrix $\left(\boldsymbol{D_I D_E}\right)^{-1}$
Step 4: $\mathbf{F}_B ds = \frac{\rho}{\Delta t}\left(\boldsymbol{D_I D_E}\right)^{-1}\left(\boldsymbol{U}_B - D_I \mathbf{u}^*\right)$
Step 5: Update the fluid force density in Eq. (7) and fluid velocity in Eq. (2b).
```

where the correlation coefficient $D_I^k D_E^i \neq 0$ requires

$$D_I\left(\boldsymbol{r}_j - \boldsymbol{X}_B^k\right) \cdot D_E\left(\boldsymbol{r}_j - \boldsymbol{X}_B^i\right) \neq 0. \tag{15}$$

Therefore, Eq. (15) can be satisfied with following relationships as:

$$D_I\left(\boldsymbol{r}_j - \boldsymbol{X}_B^k\right) \neq 0, \quad D_E\left(\boldsymbol{r}_j - \boldsymbol{X}_B^i\right) \neq 0. \tag{16}$$

Assuming there are two sets of Eulerian grid points: $j \in R(p)$ and $j \in R(q)$ to satisfy $D_I\left(\boldsymbol{r}_j - \boldsymbol{X}_B^k\right) \neq 0$ and $D_E\left(\boldsymbol{r}_j - \boldsymbol{X}_B^i\right) \neq 0$, respectively. Therefore, $D_I^k D_E^i \neq 0$ requires the Lagrangian points i and k to share the common Eulerian grids $j \in R(p) \cap R(q)$. Based on the 3-point delta function, when $j \in R(p)$, $\left\|\boldsymbol{r}_j - \boldsymbol{X}_B^k\right\| \leq \left\|(1.5h, 1.5h)^t\right\| = \mathcal{O}(h)$. Similarly, when $j \in R(q)$, $\left\|\boldsymbol{r}_j - \boldsymbol{X}_B^i\right\| \leq \left\|(1.5h, 1.5h)^t\right\| = \mathcal{O}(h)$.

Hence, to satisfy $D_I^k D_E^i \neq 0$, the distance between Lagrangian points i and k requires that

$$\begin{aligned}\left\|d\boldsymbol{X}_B^{ki}\right\| &= \left\|\boldsymbol{X}_B^i - \boldsymbol{X}_B^k\right\| \\ &= \left\|\left(\boldsymbol{r}_j - \boldsymbol{X}_B^i\right) - \left(\boldsymbol{r}_j - \boldsymbol{X}_B^k\right)\right\| \\ &\leq \left\|\boldsymbol{r}_j - \boldsymbol{X}_B^i\right\| + \left\|\boldsymbol{r}_j - \boldsymbol{X}_B^k\right\| \\ &\leq \left\|(3h, 3h)^T\right\| \\ &= \mathcal{O}(h).\end{aligned} \tag{17}$$

By using the second-order Taylor series expansion, the unknown terms $\mathbf{F}_B^i\left(\boldsymbol{X}_B^i\right)$ and ds^i can be expanded as:

$$\mathbf{F}_B^i = \mathbf{F}_B^k + \frac{\partial \mathbf{F}_B}{\partial \boldsymbol{X}} d\boldsymbol{X}_B^{ki} + \mathcal{O}\left(d\boldsymbol{X}_B^{ki^2}\right), \tag{18}$$

$$ds^i = ds^k + \frac{\partial ds}{\partial \boldsymbol{X}} d\boldsymbol{X}_B^{ki} + \mathcal{O}\left(d\boldsymbol{X}_B^{ki^2}\right). \tag{19}$$

Through multiplying Eqs. (18) and (19), the following equation can be obtained:

$$\begin{aligned}\mathbf{F}_B^i ds^i = {} & \mathbf{F}_B^k ds^k + \mathbf{F}_B^k \frac{\partial ds}{\partial \boldsymbol{X}} d\boldsymbol{X}_B^{ki} + \frac{\partial \mathbf{F}_B}{\partial \boldsymbol{X}} d\boldsymbol{X}_B^{ki} ds^k \\ & + \mathbf{F}_B^k \mathcal{O}\left(d\boldsymbol{X}_B^{ki^2}\right) + ds^k \mathcal{O}\left(d\boldsymbol{X}_B^{ki^2}\right) + \frac{\partial \mathbf{F}_B}{\partial \boldsymbol{X}} \frac{\partial ds}{\partial \boldsymbol{X}} \left(d\boldsymbol{X}_B^{ki}\right)^2 \\ & + \frac{\partial \mathbf{F}_B}{\partial \boldsymbol{X}} d\boldsymbol{X}_B^{ki} \mathcal{O}\left(d\boldsymbol{X}_B^{ki^2}\right) + \frac{\partial ds}{\partial \boldsymbol{X}} d\boldsymbol{X}_B^{ki} \mathcal{O}\left(d\boldsymbol{X}_B^{ki^2}\right) + \mathcal{O}\left(d\boldsymbol{X}_B^{ki^4}\right) \\ = {} & \mathbf{F}_B^k ds^k + \mathbf{F}_B^k \frac{\partial ds}{\partial \boldsymbol{X}} d\boldsymbol{X}_B^{ki} + \frac{\partial \mathbf{F}_B}{\partial \boldsymbol{X}} d\boldsymbol{X}_B^{ki} ds^k + \mathcal{O}\left(d\boldsymbol{X}_B^{ki^2}\right).\end{aligned} \tag{20}$$

The spacing of the Lagrangian points should be close to the background Eulerian grid spacing to ensure that the appropriate correlation between Lagrangian and Eulerian points is achieved as follows:

$$ds = \mathcal{O}(h). \tag{21}$$

Besides, the force density at the Lagrangian points is $\mathbf{F}_B = \rho\left(\boldsymbol{U}_B - D_I \mathbf{u}^*\right)/\Delta t$. Owing to that the smoothed delta function D_I is first-order accurate, the following relationship can be derived as:

$$\mathbf{F}_B = \mathcal{O}(h). \tag{22}$$

Substituting Eqs. (21) and (22) into Eq. (20), the second and third terms of the RHS terms in Eq. (20) should satisfy the following relationships as:

$$\begin{aligned}\left\|\mathbf{F}_B^k \frac{\partial ds}{\partial \boldsymbol{X}} d\boldsymbol{X}_B^{ki}\right\| &\leq \left\|\frac{\partial ds}{\partial \boldsymbol{X}}\right\| \left\|d\boldsymbol{X}_B^{ki}\right\| \left\|\mathbf{F}_B^k\right\| \\ &= \left\|\frac{\partial ds}{\partial \boldsymbol{X}}\right\| \cdot \mathcal{O}(h) \cdot \mathcal{O}(h) \\ &= \mathcal{O}\left(h^2\right),\end{aligned} \tag{23}$$

$$\begin{aligned}\left\|\frac{\partial \mathbf{F}_B}{\partial \boldsymbol{X}} d\boldsymbol{X}_B^{ki} ds^k\right\| &\leq \left\|\frac{\partial \mathbf{F}_B}{\partial \boldsymbol{X}}\right\| \left\|d\boldsymbol{X}_B^{ki}\right\| \left\|ds^k\right\| \\ &= \left\|\frac{\partial \mathbf{F}_B}{\partial \boldsymbol{X}}\right\| \cdot \mathcal{O}(h) \cdot \mathcal{O}(h) \\ &= \mathcal{O}\left(h^2\right).\end{aligned} \tag{24}$$

Substituting Eqs. (23) and (24) into Eq. (20), when $D_I^k D_E^i \neq 0$, the following second-order approximation can be obtained:

$$\mathbf{F}_B^i ds^i = \mathbf{F}_B^k ds^k + \mathcal{O}(h^2). \tag{25}$$

Substituting Eq. (25) into Eq. (14), the Lagrangian force density can be approximately predicted with second-order accuracy as:

$$\mathbf{F}_B^k ds^k = \frac{\frac{\rho}{\Delta t}\left(\boldsymbol{U}_B^k - D_I^k \mathbf{u}^*\right)}{\sum_{i \in D_I^k D_E^i \neq 0}\left(D_I^k D_E^i\right)} + \mathcal{O}(h^2). \tag{26}$$

Subsequently, the explicit boundary thickening direct forcing IBM is developed based on the second order approximation. The procedure of the explicit BTDF-IB is given in **Algorithm2**. With the help of the second-order approximation, the explicit BTDF-IB can resolve large FSI problems with second-order spatial accuracy. In Section 4, the numerical tests with the proposed explicit BTDF-IB will corroborate whether the boundary velocity errors are indeed within $\mathcal{O}(h^2)$.

3.2. Comparisons of the memory consumption and computational cost between implicit and explicit BTDF-IBs

The amount of Lagrangian points required for practical three-dimensional FSI problems grows with the complexity of the geometries involved to ensure that proper correlation is established between the Lagrangian and Eulerian points. Therefore, it is expected that the original implicit BTDF-IB would need a much larger amount of memory than the explicit BTDF scheme proposed in this study, as the former approach requires the construction of the correlation matrix and the inversion of the $D_I D_E$. However, the exact amount of computational cost saving is not known. Hence, the original implicit BTDF scheme and the proposed explicit BTDF scheme are compared in terms of memory and computational time consumption.

In this section, all test cases are conducted on the same Eulerian meshes of 240^3, where the number of the Lagrangian points is increased from 10^3 to 2×10^4. Tables 1 and 2 present the comparisons of memory consumption and computational time between the implicit and explicit BTDF-IBs, respectively. Following the **Algorithm1** and **Algorithm2**, the implicit scheme would require N_L times memory space more than that of the proposed explicit scheme, demonstrating that the proposed explicit BTDF-IB can be utilized to solve practical FSI problems with a large number of Lagrangian points. Table 2 shows that the proposed explicit BTDF-IB is more efficient than the original implicit scheme; therefore, the proposed explicit BTDF-IB can efficiently simulate FSI problems with multiple objects and complex geometries.

4. Results and discussion

In this section, the overall accuracy of the proposed explicit BTDF-IB integrated with the RLBFS is assessed through two-dimensional decaying flow. In addition, the capability and robustness of the proposed explicit BTDF-IB are evaluated by the numerical examinations of flow past an in-line oscillating cylinder, particle sedimentation, and flow past a 3D flexible plate, where complex geometries, moving boundaries

Algorithm 2 The explicit BTDF-IB

```
Step 1: $\boldsymbol{D}_I$ and $\boldsymbol{D}_E$
Step 2: $\zeta_k = \sum D_I^k D_E^i$
Step 3: $\mathbf{F}_B ds = \frac{\rho}{\Delta t}\left(\boldsymbol{U}_B - D_I \mathbf{u}^*\right)/\zeta$
Step 4: Update the fluid force density in Eq. (7) and fluid velocity in Eq. (2b).
```

Table 1
Comparison of the virtual memory for storing the variables related to IBM of implicit and explicit BTDF-IBs. For implicit BTDF-IB, it requires $N_L \times N_L$ memory space to store $\boldsymbol{D}_I\boldsymbol{D}_E$; for explicit BTDF-IB, it requires N_L memory space to store ζ.

Number of Lagrangian points	Algorithm		Ratio
	Implicit BTDF	Explicit BTDF	
1000	7.6294 MB	7.8125 KB	1000
5000	190.7349 MB	39.0625 KB	5000
10000	762.9395 MB	78.125 KB	10 000
15000	1716.6138 MB	117.1875 KB	15 000
20000	3051.7578 MB	156.25 KB	20 000

Table 2
Comparison of the time consumption of implicit and explicit BTDF IBM procedures for one time step with single CPU processor (2.3 GHz).

Number of Lagrangian points	Algorithm		Ratio
	Implicit BTDF	Explicit BTDF	
1000	4.04688 s	0.17188 s	23.545
5000	2276.59375 s	3.85938 s	589.887
10000	22646.76563 s	15.00000 s	1509.784
15000	83489.26563 s	32.60938 s	2560.284
20000	210899.28125 s	55.29688 s	3813.946

and large deformations are involved. The numerical results demonstrate that the proposed explicit-IB can accurately predict the nonlinear dynamic characteristics of complex FSI systems.

4.1. Numerical test of overall accuracy

In this subsection, the overall accuracy of the implicit and explicit BTDF-IBs with the RLBFS are evaluated by using two-dimensional decaying vortex flow. This benchmark case has been widely adopted to analyze the overall order of accuracy in IB-NS [42] and IB-LBM [49]. The analytical solution of this problem is provided as:

$$u = -u_0 \cos(\pi x/L)\sin(\pi y/L)\, e^{-\frac{2\pi^2 u_0 t}{\mathrm{Re}\, L}}, \tag{27a}$$

$$v = u_0 \sin(\pi x/L)\cos(\pi y/L)\, e^{-\frac{2\pi^2 u_0 t}{\mathrm{Re}\, L}}, \tag{27b}$$

$$p = p_0 - \frac{\rho_0 u_0^2}{4}\left[\cos(2\pi x/L) + \cos(2\pi y/L)\right] e^{-\frac{4\pi^2 u_0 t}{\mathrm{Re}\, L}}, \tag{27c}$$

where ρ_0 is the fluid density, u_0 denotes the characteristic velocity, and p_0 is the reference pressure. The computational domain is $[-L,\ L] \times [-L,\ L]$ with periodic boundary condition enforced on the domain boundaries. A circular cylinder with radius of $0.5L$ is immersed at the center of the computational domain, where the exact velocity solutions are imposed on the cylinder's surface. In this problem, the Reynolds number $Re = u_0 L/\nu = 20$ and the parameters $\Delta t = 0.5$, $\Delta x = 1$, $c_s = 1/\sqrt{3}$, and $\nu = 0.05$ are employed. Five different sets of mesh, namely, 40^2, 60^2, 80^2, 100^2, and 120^2 are adopted to discretize the computational domain to examine the convergence order. The analytical solutions at $t^* = u_0 t/L = 0$ is adopted as the initial condition and the relative errors ε_{u2} and ε_{v2} are calculated at $t^* = 1$ through the following expressions:

$$\varepsilon_{u2} = \sqrt{\frac{\sum_{i=1}^{N\times N}\left[\frac{(u^n - u^a)}{u_0}\right]^2}{N\times N}}, \quad \varepsilon_{v2} = \sqrt{\frac{\sum_{i=1}^{N\times N}\left[\frac{(v^n - v^a)}{u_0}\right]^2}{N\times N}}, \tag{28}$$

where the superscripts, n and a, represent the numerical results and analytical solutions, respectively.

Fig. 2 presents the relative errors on different mesh spacings. It can be seen that both the explicit and implicit BTDF-IBs with RLBFS exhibit second order spatial accuracy and the second order approximation in explicit BTDF-IB has negligible effects on the global order of accuracy.

4.2. Flow past an in-line oscillating cylinder

In this subsection, an in-line oscillating cylinder in a free stream at $Re = U_0 D/\nu = 100$ is adopted to test the capability of the explicit BTDF-IB in solving moving boundary problems, where U_0 and D are the free stream velocity and the cylinder diameter, respectively. The computational domain of $[-14D, 20D] \times [-15D, 15D]$ is discretized by a non-uniform mesh size of 700×900, where the sub-domain around the oscillating cylinder $[-1D, 4D] \times [-4D, 4D]$ is discretized by a uniform mesh with a mesh spacing of $h = 0.01D$. The immersed cylinder is discretized by 314 Lagrangian points to construct a proper correlation between the Lagrangian and Eulerian points. The oscillating motion is governed by:

$$X_c(t) = A\sin\left(2\pi f_c t\right), \tag{29}$$

where A and f_c are the oscillating amplitude and frequency, respectively. In this problem, $A/D = 0.14$ and $f_c = 2f_0$ are adopted, where f_0 denotes the vortex shedding frequency of a stationary cylinder at $Re = 100$. Therefore, the oscillating period is $T_c = 1/f_c$.

Fig. 3 presents the comparisons of the instantaneous vorticity contours of the in-line oscillating cylinder between the reference contours of Luo et al. [60] and the present results at four time instants. As shown in Fig. 3, the results obtained by the proposed explicit BTDF-IB are in a good agreement with those of Luo et al. [60], and the instantaneous vorticity contours predicted by the proposed explicit BTDF-IB are the same as those of the implicit scheme, demonstrating the capability of the proposed explicit BTDF-IB in imposing the no-slip boundary condition on moving boundaries.

To quantitatively examine the accuracy and capability of the proposed explicit BTDF-IB, the comparisons of the time histories of the drag and lift coefficients are shown in Fig. 4. It can be seen that the time evolutions of the drag and lift coefficients agree well with those of Luo et al. [60], indicating that the proposed explicit BTDF-IB is capable of accurately predicting the nonlinear dynamic characteristics of this problem. In addition, the hydrodynamic forces generated by the proposed explicit BTDF-IB are the same as those of the implicit scheme, demonstrating that the second order approximation has negligible effects on the numerical solutions. To further assess the accuracy of the proposed method, Table 3 compares the time-averaged drag force and the maximum lift force with that of previous studies [46,61,62]. It is evident from Table 3 that the present results are consistent with the reference data and the quantitative statistical results generated by the proposed explicit BTDF-IB are the same as those of the implicit scheme, which further confirms the suitability of the second-order approximation.

The instantaneous boundary velocity errors defined as: $\Delta U_x = U_B - D_I\mathbf{u}$ and $\Delta U_y = V_B - D_I\mathbf{u}$ are examined in Fig. 5 to ensure that the no-slip boundary condition is satisfied by the proposed explicit BTDF-IB. Do note that the selected time instants in Fig. 5 are identical to those results presented in Fig. 3. It is evident from Fig. 5 that the boundary velocity errors of the proposed explicit BTDF-IB are relatively small and within $\mathcal{O}\left(h^2\right)$, demonstrating that the proposed explicit BTDF-IB can efficiently impose the no-slip boundary condition on the surface of moving objects and maintain similar accuracy as the implicit scheme.

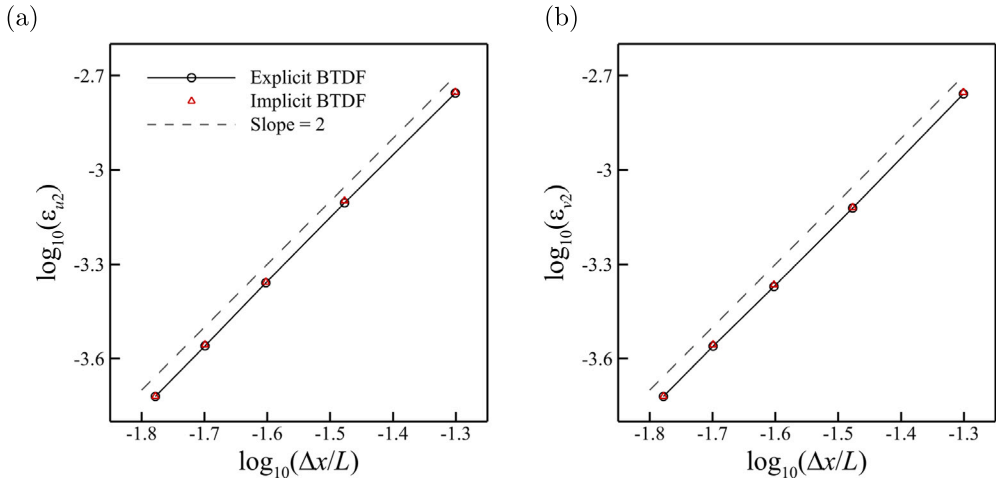

Fig. 2. Grid convergence of the implicit and explicit BTDF-IBs: (a) L_2 norm of error for u; (b) L_2 norm of error for v. Both the implicit and explicit BTDF-IBs present second-order spatial accuracy, and the second-order approximation in explicit BTDF-IB has negligible effects on the overall accuracy.

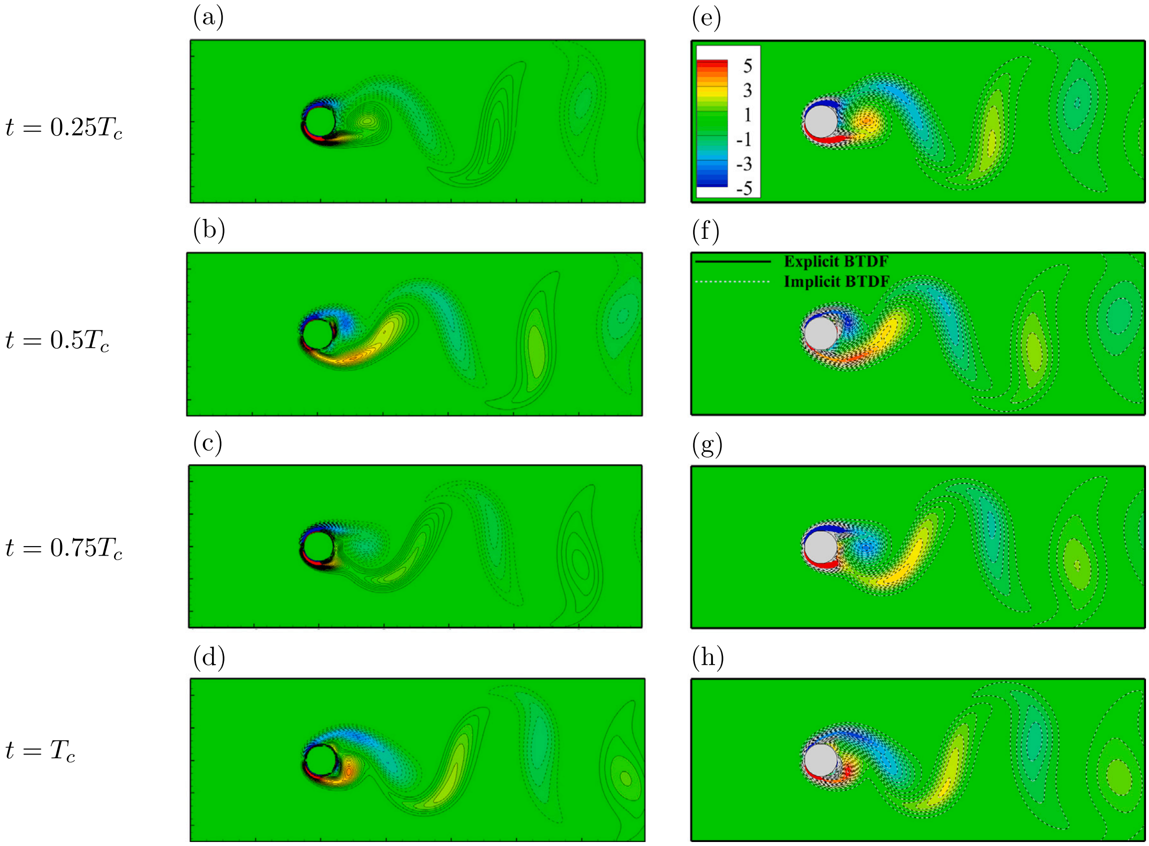

Fig. 3. Comparisons of instantaneous vorticity contours around the in-line oscillating cylinder. Left column: reference contours of Luo et al. [60]; right column: background contours with black solid lines generated by the explicit BTDF-IB and the contours with gray dotted lines provided by the implicit BTDF-IB. The numerical results generated by the proposed explicit BTDF-IB agree well with those of Luo et al. [60], and the instantaneous vorticity contours predicted by the proposed explicit BTDF-IB are identical to those of the implicit scheme, indicating that the proposed explicit BTDF-IB can accurately enforce the no-slip boundary condition on moving boundaries.

4.3. Sedimentation of a circular particle in a tank

In this subsection, the proposed explicit BTDF-IB is employed to investigate the hydrodynamic performance of a free falling circular particle. This simulation can be considered to be a quite challenging FSI problem [57,63–65], especially for numerical approaches with body-fitted grid due to the large dynamic motions involved. In this problem, the size of the rectangular computational domain is 2 cm × 6 cm, where the fluid density is $\rho_f = 1.0$ g/cm^3 and the dynamic viscosity is $\mu =$ 0.1 g/(cm s). The circular particle with diameter of $D = 0.25$ cm and density of $\rho_p = 1.25$ g/cm^3 is released at (1 cm, 4 cm). The computational domain is discretized by a Cartesian mesh of 200 × 600 with grid spacing of $h = 0.01$ cm, and the particle surface is discretized by 78 Lagrangian points to ensure $ds = \mathcal{O}(h)$.

Fig. 6 shows the vortical structures around the falling particle, where the vortical strength is enhanced by the accelerated motion. The evolution of the vertical position Y_p, the vertical velocity V_p, the particle Reynolds number $Re_p = \rho_p D_p \sqrt{U_p^2 + V_p^2}/\mu$, and the translation

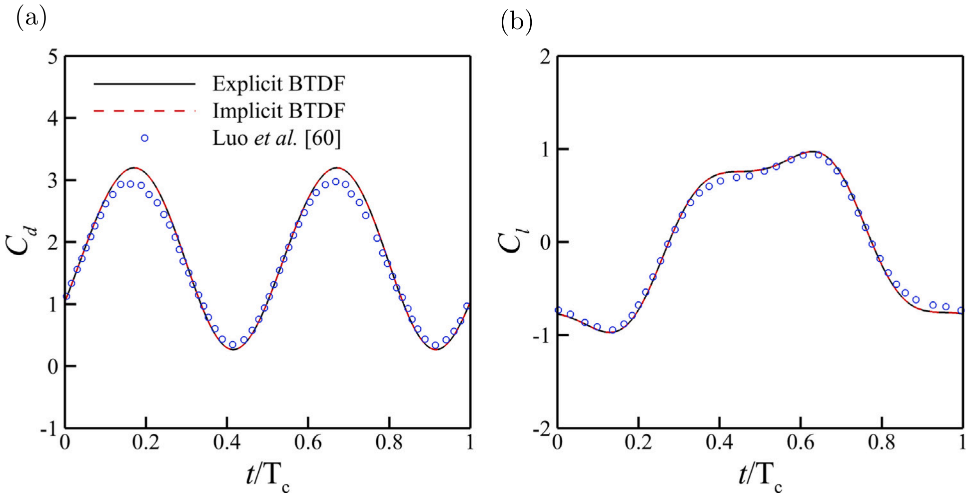

Fig. 4. Comparisons of the time evolutions of the (a) drag and (b) lift coefficients for the in-line oscillating cylinder in a free stream at $Re = 100$. The time evolutions of the drag and lift coefficients predicted by the proposed explicit BTDF-IB agree well with those of Luo et al. [60], indicating that the explicit BTDF-IB can accurately predict the nonlinear dynamic characteristics of FSI problems with moving boundaries. Additionally, the hydrodynamic forces generated by the proposed explicit BTDF-IB are identical to those of the implicit scheme, demonstrating that the second order approximation has negligible effects on the predicted solutions.

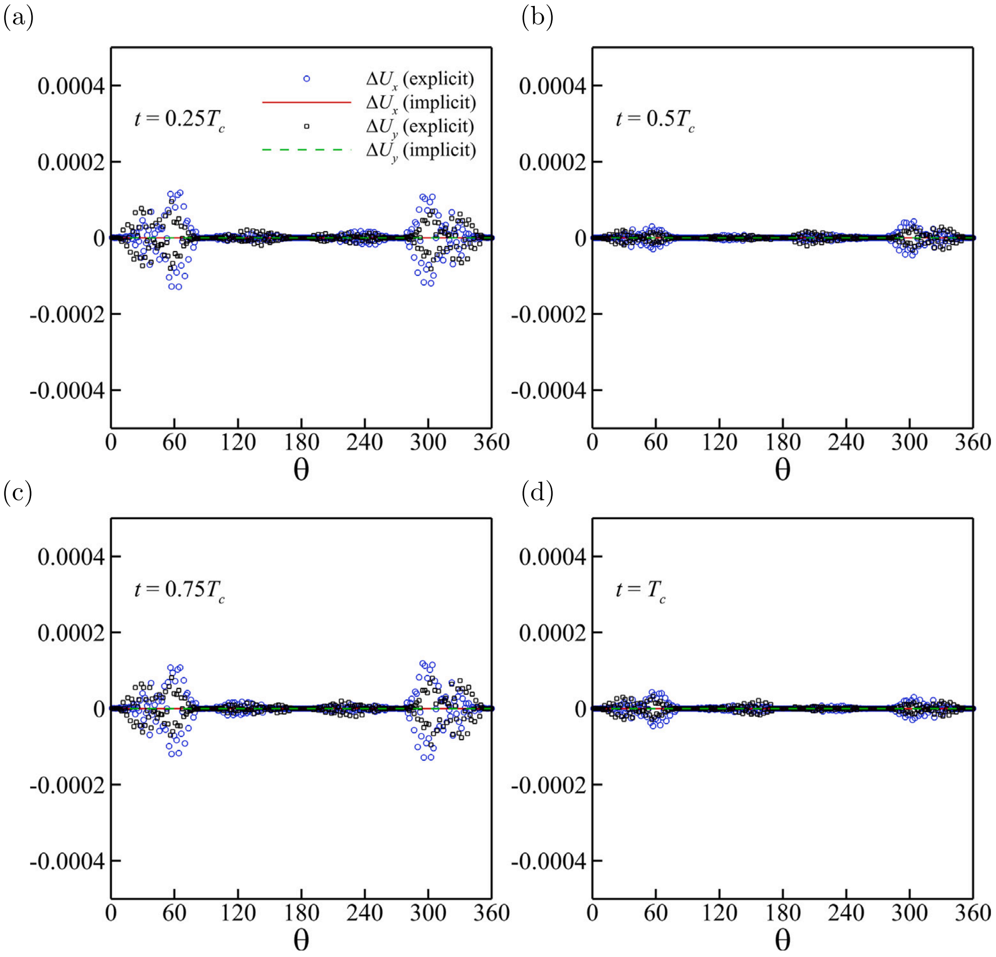

Fig. 5. The instantaneous boundary velocity errors of the explicit and implicit BTDF-IBs. (a) $t = 0.25T_c$, (b) $t = 0.5T_c$, (c) $t = 0.75T_c$, and (d) $t = T_c$. The instantaneous boundary velocity errors of the proposed explicit BTDF-IB are relatively small and confined to $\mathcal{O}(h^2)$, indicating that the proposed explicit BTDF-IB can efficiently impose the no-slip boundary condition on moving boundaries and maintain similar accuracy as the implicit scheme.

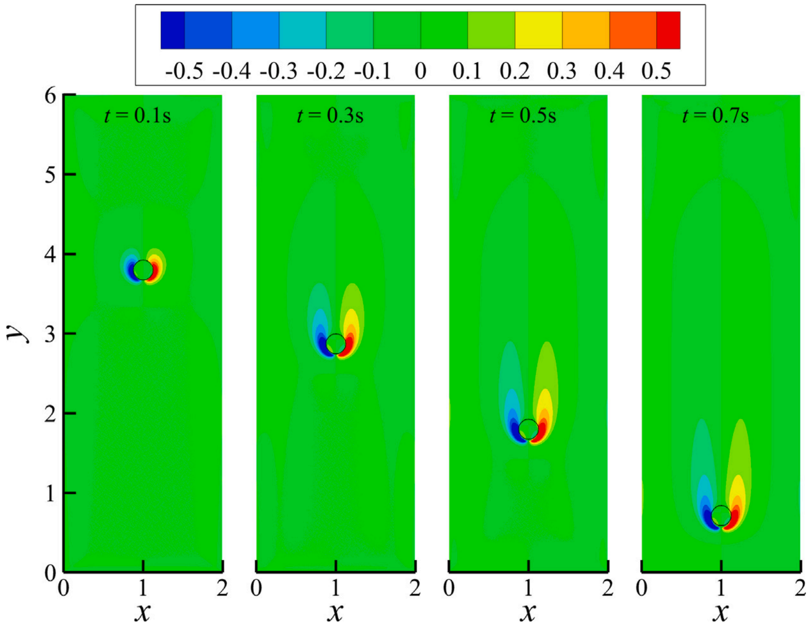

Fig. 6. The vortical structures around the falling particle at different time instants generated by the proposed explicit BTDF-IB. It can be seen that the vortical strength is enhanced by the accelerated falling motion.

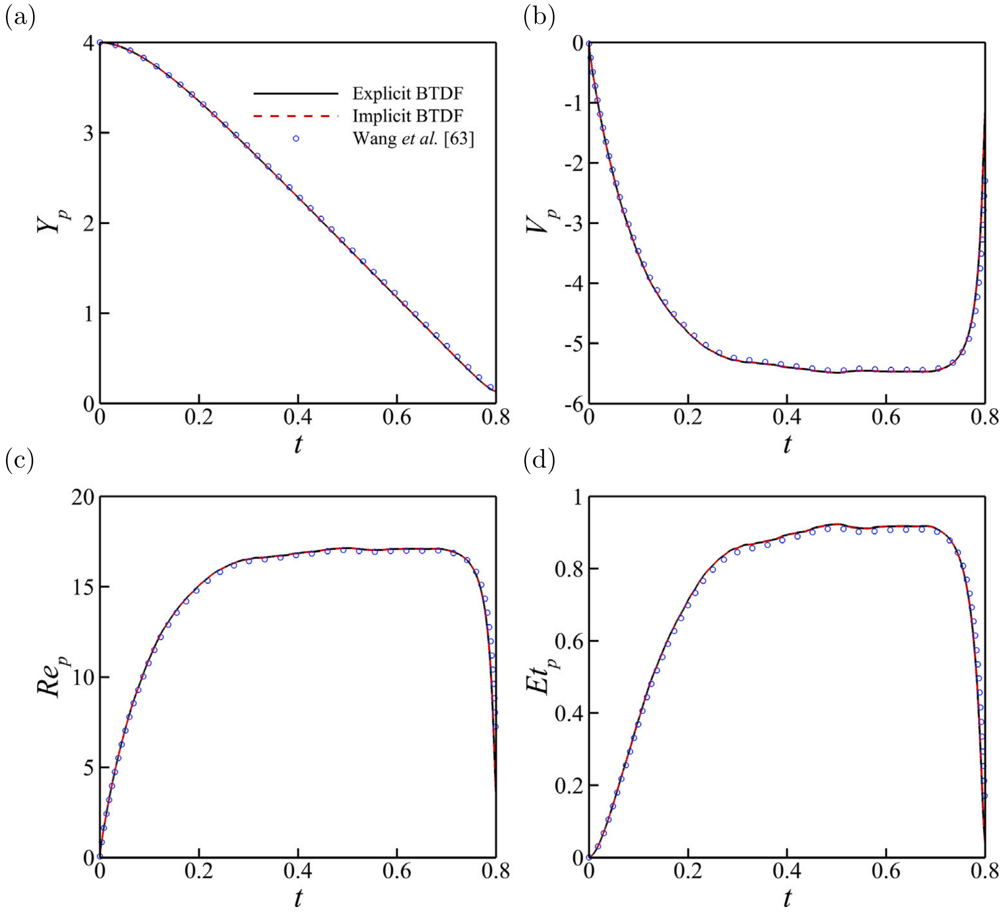

Fig. 7. Comparison of four quantities for a free falling particle: (a) vertical position, (b) vertical velocity, (c) particle Reynolds number, and (d) translational kinetic energy. The predicted results agree well with the previous study [63] and the difference between the results generated by the explicit and implicit BTDF-IBs are negligible, demonstrating that the proposed explicit BTDF-IB can accurately resolve the dynamic response of FSI problems with moving boundaries and can be extended to investigate particle-laden flows.

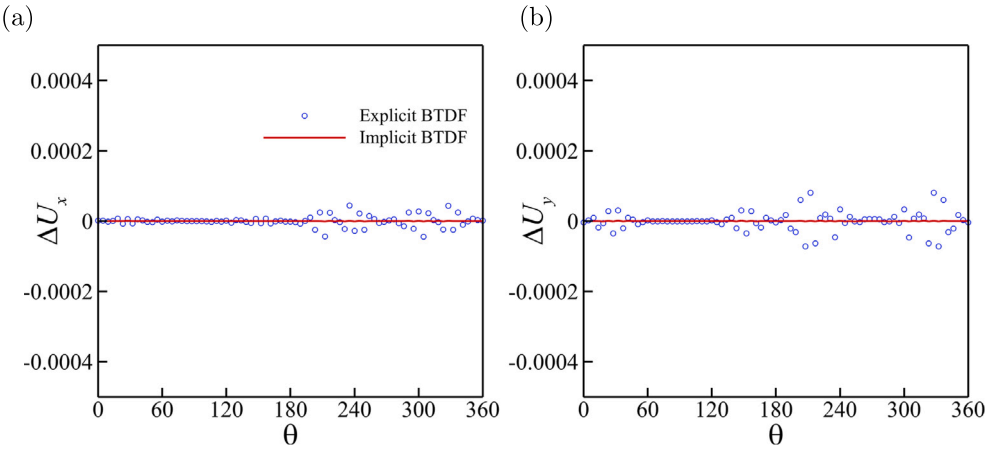

Fig. 8. The boundary velocity errors at $t = 0.3$ s: (a) the horizontal velocity error ΔU_x and (b) the vertical velocity error ΔU_y, where $\Delta U_x = U_p - \boldsymbol{D_I}\mathbf{u}$ and $\Delta U_y = V_p - \boldsymbol{D_I}\mathbf{u}$ are defined. The numerical results indicate that the proposed explicit BTDF-IB can accurately enforce the no-slip boundary condition and the instantaneous boundary velocity errors are confined to $\mathcal{O}\left(h^2\right)$ governed by the second-order approximation.

Table 3
Comparison of drag and lift coefficients for the in-line oscillating cylinder in a free stream at $Re = 100$.

$Re = 100$	f_c/f_0	$C_{d,mean}$	$C_{l,max}$
Örley et al. [61]	2	1.73	0.93
Su et al. [46]	2	1.7	0.97
Liao et al. [62]	2	1.71	0.95
Implicit BTDF	2	**1.75**	**0.97**
Explicit BTDF	2	**1.75**	**0.97**

kinetic energy $Et_p = \rho_p \pi D^2 \left(U_p^2 + V_p^2\right)/4$ are computed and shown in Fig. 7 to quantitatively examine the accuracy and the capability of the proposed explicit BTDF-IB. It is evident from Fig. 7 that the present results agree well with previous study [63] and the difference between the results generated by the explicit and implicit BTDF-IBs are negligible, indicating that the proposed explicit BTDF-IB can accurately resolve the dynamic response of FSI problems with moving boundaries and can be extended to simulate particle-laden flows.

To quantitatively examine whether the boundary velocity satisfies the no-slip boundary condition, the horizontal and vertical velocity errors are plotted in Fig. 8, which are defined as: $\Delta U_x = U_p - \boldsymbol{D_I}\mathbf{u}$ and $\Delta U_y = V_p - \boldsymbol{D_I}\mathbf{u}$. It can be seen that the proposed explicit BTDF-IB can accurately enforce the no-slip boundary condition and the small velocity errors are within $\mathcal{O}\left(h^2\right)$ governed by the second-order approximation.

4.4. A 3D flexible plate flapping in a free stream

In this subsection, a 3D flexible plate in a uniform flow is simulated to assess the accuracy and capability of the proposed explicit BTDF-IB in solving three-dimensional FSI problems. This problem not only involves complex geometries, but also moving boundaries with large deformations, providing an ideal opportunity to test the effectiveness of the proposed explicit BTDF-IB in enforcing the no-slip boundary condition for complex FSI problems. As shown in Fig. 9, the 3D flexible plate with a length L is flapping in a uniform flow. The governing equation of the 3D flexible plate can be written in a curvilinear coordinate form [66] as:

$$\rho_s \frac{\partial^2 \mathbf{X}}{\partial t^2} = \sum_{i,j=1}^{2} \left[\frac{\partial}{\partial s_i} \left(\sigma_{ij} \frac{\partial \mathbf{X}}{\partial s_j} \right) - \frac{\partial^2}{\partial s_i \partial s_j} \left(\kappa_{ij}^b \frac{\partial^2 \mathbf{X}}{\partial s_i \partial s_j} \right) \right] + \boldsymbol{F}_f, \tag{30}$$

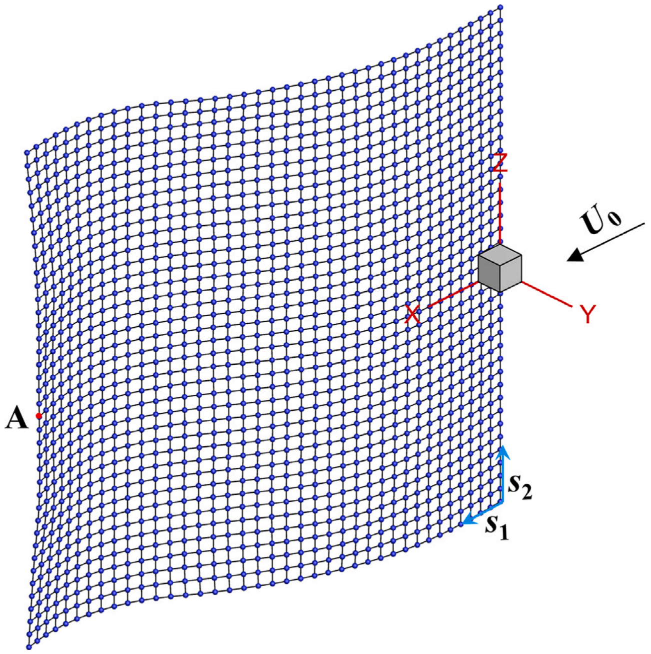

Fig. 9. Schematic view of the 3D flexible plate in a uniform flow, where the red point A is the midpoint on the trailing edge and the leading edge's center is located at the origin of the domain. The local curvilinear coordinate system is formed along the s_1 and s_2 directions.

where ρ_s, $\mathbf{X}$, $\boldsymbol{F}_f$ denote the area density of the 3D plate, the location of the Lagrangian points (see the blue points indicated in Fig. 9), and the fluid force, respectively. σ_{ij} is defined as

$$\sigma_{ij} = \varphi_{ij} \left(\frac{\partial \mathbf{X}}{\partial s_i} \cdot \frac{\partial \mathbf{X}}{\partial s_j} - \Gamma_{ij}^0 \right), \tag{31a}$$

$$\Gamma_{ij}^0 = \begin{cases} 1, if\ i = j, \\ 0, if\ i \neq j. \end{cases} \tag{31b}$$

When $i = j$, φ_{ij} and κ_{ij}^b denote the tension and bending coefficients, respectively; otherwise, they both represent the shearing and twisting coefficients, respectively. Details on solving the governing equation Eq. (30) can be found in [67].

In this problem, the governing dimensionless parameters are the Reynolds number $Re = U_0 L/\nu$, the mass ratio $\Theta = \rho_s/(\rho L)$, the dimensionless stretching and shearing coefficients $\boldsymbol{\Phi}_{ij} = \varphi_{ij}/(\rho_s U_0^2)$, and the dimensionless bending and twisting coefficients $K_{ij} = \kappa_{ij}^b/(\rho_s U_0^2 L^2)$,

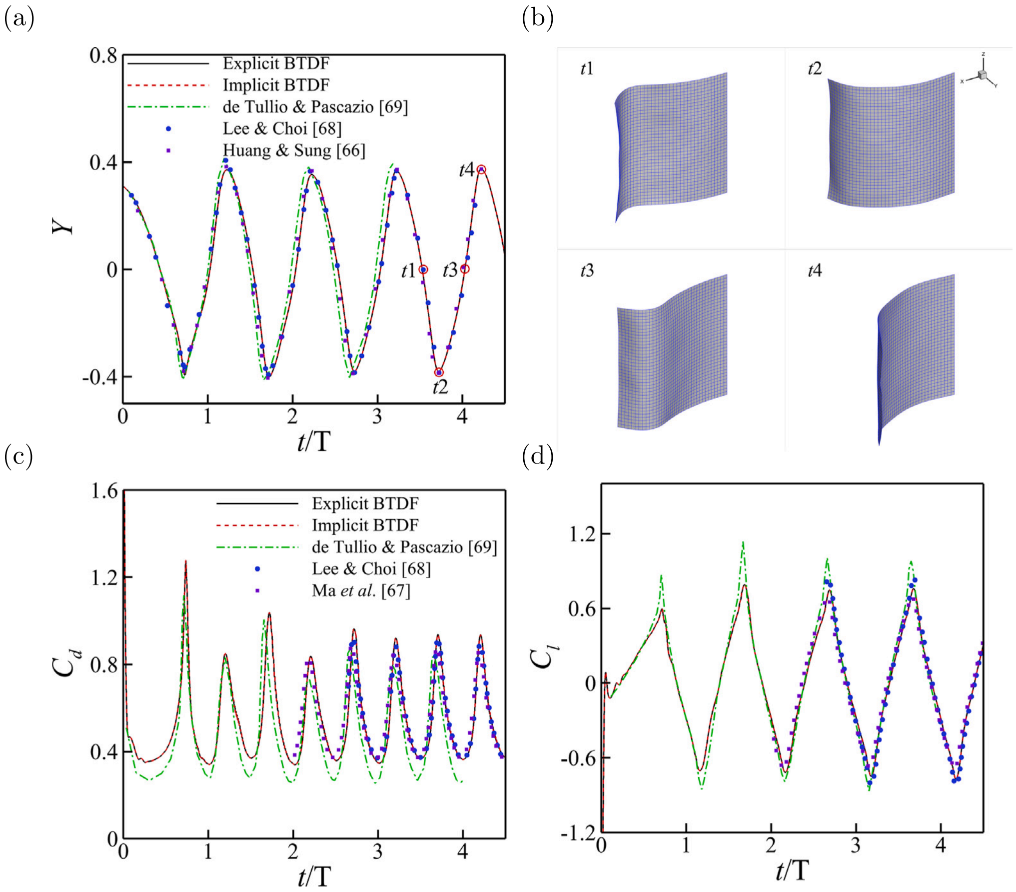

Fig. 10. (a) The comparison of the transverse displacement of the point A (see Fig. 9), and (b) the instantaneous geometries of the 3D flexible plate at four time instants as labeled in Fig. 10(a). Comparisons of (c) the drag coefficient and (d) the lift coefficient. Note that Figs. 10(c) and 10(d) share the same legend. The numerical results predicted by the implicit and explicit BTDF-IBs agree well with each other and also with reference data [66–69], demonstrating that the implicit and explicit BTDF-IBs can both accurately predict the nonlinear characteristics of a fully coupled fluid–structure system. Furthermore, the numerical results shows that both the implicit and explicit BTDF-IBs yield almost identical solutions, indicating that the second-order approximation proposed in this study has negligible effects on the quantitative results and the flow physics.

where U_0 denotes the free stream velocity. The dimensionless parameters chosen for this problem are $Re = 200$, $\Theta = 1$, $\Phi_{11} = \Phi_{22} = 10^3$, $\Phi_{12} = 10$, and $K_{11} = K_{22} = K_{12} = 10^{-4}$. The computational domain is set as $[-2L, 7L]$, $[-4L, 4L]$, and $[-1L, 1L]$ along the x, y, and z direction, respectively; where the fluid region ($[-0.2L, 1.3L] \times [-0.7L, 0.7L] \times [-0.7L, 0.7L]$) around the 3D flexible plate is uniformly discretized with a finer mesh spacing of $h = L/75$ to capture the dynamic interactions between the 3D plate and the surrounding flows. As shown in Fig. 9, the 3D plate is uniformly discretized by 1521 Lagrangian points with grid spacing of $L/38$, where the leading edge is pinned and the other three edges are enforced with free moving boundary condition. At the inflow boundary, the Dirichlet boundary conditions ($u_x = U_0$, $u_y = u_z = 0$) are applied; the Neumann boundary conditions ($\partial \mathbf{u}/\partial n = 0$) are enforced at the outflow boundary and the four side walls.

Fig. 10 presents the comparisons of the quantitative results, such as the transverse displacement of the midpoint A on the trailing edge, the drag and lift coefficients. It can be seen that the results predicted by the implicit and explicit BTDF-IBs agree well with each other and also with reference data [66–69], indicating that the implicit and explicit BTDF-IBs can both accurately predict the nonlinear characteristics of a fully coupled fluid–structure system. Furthermore, the results shows that both the implicit and explicit BTDF-IBs yield almost identical solutions, demonstrating that the second-order approximation proposed in this study has negligible effects on the quantitative results and the flow physics. Fig. 10(b) shows the instantaneous geometries of the 3D flexible plate at four time instants as labeled in Fig. 10(a), where a longitudinal traveling wave is clearly observed as the plate deforms. Table 4 tabulates the quantitative comparisons of flapping amplitude and Strouhal number, and the results predicted by the implicit and explicit BTDF-IBs are in good agreement with the reference data [66,68–70].

Table 4
Comparison of the flapping amplitude A/L and the Strouhal number $St = fL/U_0$, where f denotes the flapping frequency.

$Re = 200$	Amplitude A/L	Strouhal number St
Lee & Choi [68]	0.752	0.265
de Tullio & Pascazio [69]	0.795	0.265
Tian et al.- Flag 2 [70]	0.806	0.266
Huang & Sung [66]	0.780	0.260
Implicit BTDF	**0.756**	**0.260**
Explicit BTDF	**0.758**	**0.260**

Fig. 11 shows the instantaneous vortical structures around the 3D flapping plate, where the shedding vortex from the trailing edge is merged with the vortices shedding from the side edges to form a hairpin-like vortical structure in the wake region. These numerical observations are consistent with previous studies [66,68–70], qualitatively validating the feasibility of the proposed explicit BTDF-IB for predicting the nonlinear characteristics of a fully coupled fluid–structure systems.

As shown in Fig. 12, the instantaneous boundary velocity errors at four selected time instants (labeled in Fig. 10(a)) are computed to examine if the no-slip boundary condition is fully enforced on the 3D flexible plate by the proposed explicit BTDF-IB. The boundary velocity

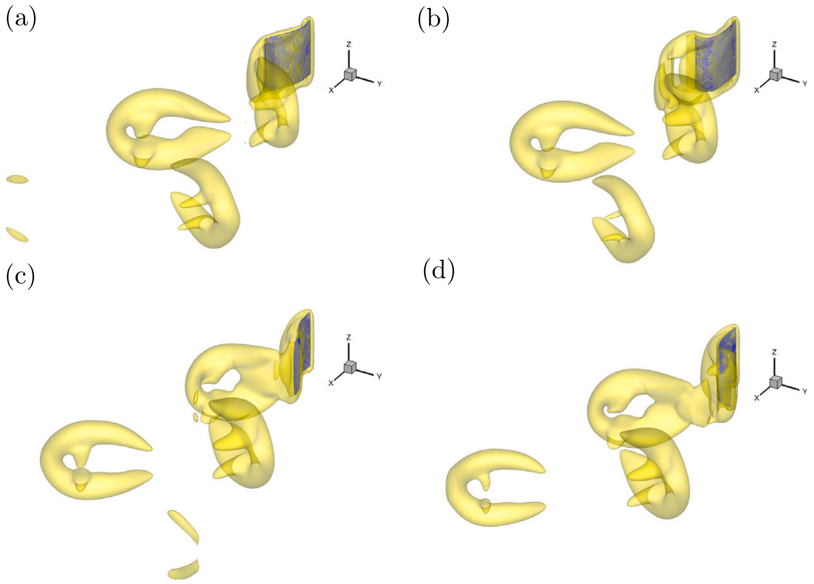

Fig. 11. The vortical structures around the 3D flexible plate at different time instants, where the vortical structures are characterized by the Q-criterion of $Q = 0.2$. (a) $t = 87$ s, (b) $t = 87.6$ s, (c) $t = 88.8$ s, and (d) $t = 89.4$ s. A hairpin-like vortical structure in the wake region is clearly observed, which is consistent with previous studies [66,68–70].

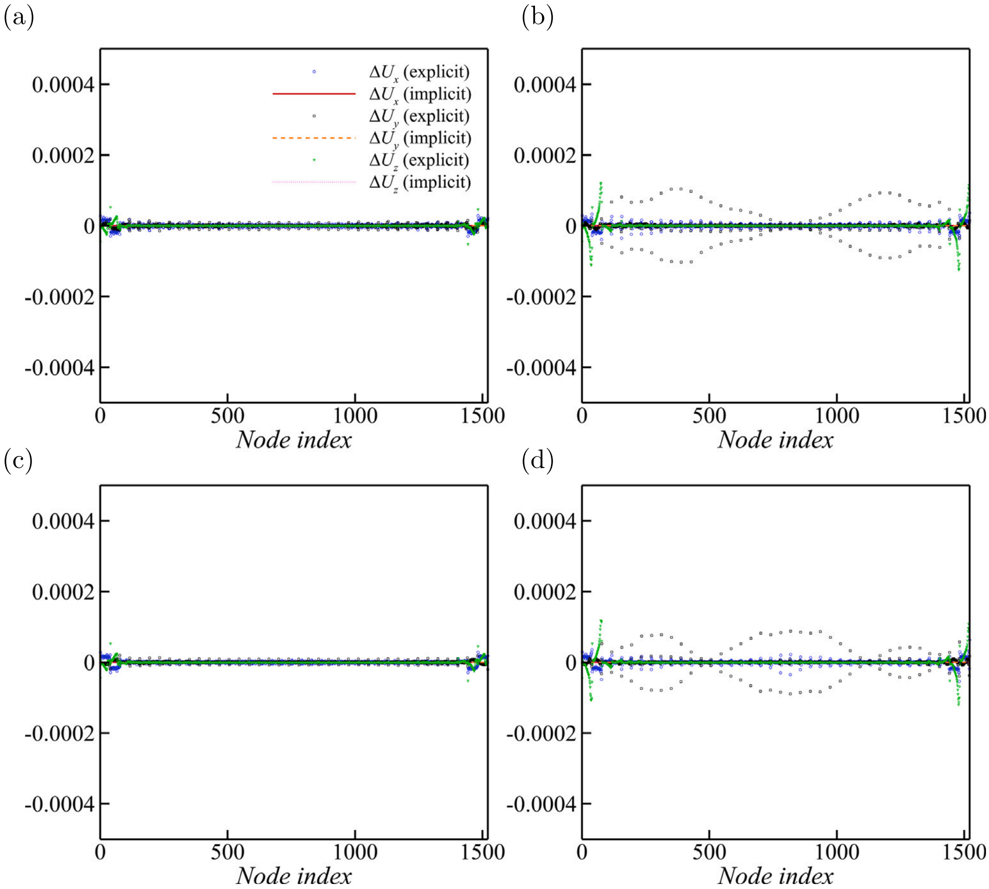

Fig. 12. The instantaneous boundary velocity errors of 1521 Lagrangian points at four time instants as labeled in Fig. 10(a). (a) $t1$, (b) $t2$, (c) $t3$, and (d) $t4$. The boundary velocity errors are defined as: $\Delta U_x = U_B - D_I\mathbf{u}$, $\Delta U_y = V_B - D_I\mathbf{u}$ and $\Delta U_z = W_B - D_I\mathbf{u}$. The instantaneous boundary velocity errors at four time instants are confined to $\mathcal{O}(h^2)$, which is consistent with the proposed second-order approximation. It demonstrates that the proposed explicit BTDF-IB can accurately enforce the no-slip boundary condition in FSI problems with moving boundaries and large deformations. Therefore, the explicit BTDF scheme can achieve similar accuracy as the implicit BTDF scheme with significant saving in computational cost.

errors are relatively small when the trailing edge is at the neutral position, but fluctuate noticeably as it reaches its maximum transverse position. These boundary velocity errors' fluctuations may be attributed to the rapid deformations at time instants $t2$ and $t4$. Note that the boundary velocity errors at all time instants are well within $\mathcal{O}(h^2)$, which is consistent with the second-order approximation. Therefore, the explicit BTDF scheme can achieve similar accuracy as the implicit BTDF scheme with significant saving in computational cost. This makes the proposed explicit BTDF scheme a promising alternative for simulating complex fluid–structure interaction problems.

5. Conclusions

In this work, the explicit boundary thickening direct forcing immersed boundary method is proposed with a proper correlation between the thicknesses of solid and fluid forcing shells, eliminating the needs of significant memory requirements and reducing the computational costs in the original implicit direct forcing scheme. Using Taylor series expansion, a second-order approximation is derived through the error analysis to eliminate the needs of constructing and inversing a large correlation matrix in the implicit direct forcing scheme while maintaining similar accuracy to the implicit scheme. The proposed explicit and implicit BTDF-IBs are coupled with RLBFS to solve FSI related problems through the prediction and forcing steps.

The proposed explicit and implicit BTDF schemes are validated with several classical benchmarks. The numerical accuracy test indicates that the overall accuracy of the explicit and implicit BTDF-IBs with RLBFS are of second order accurate in space. The good agreement between the numerical results predicted by the explicit BTDF-IB and reference data further demonstrates the feasibility and robustness of the proposed explicit BTDF scheme. Moreover, the numerical solutions generated by the proposed explicit BTDF scheme are almost identical to the implicit BTDF scheme in all test cases, indicating that the second-order approximation has negligible effects on the global accuracy. Most importantly, the results obtained from a 3D flexible plate flapping in a free stream demonstrate that the explicit BTDF scheme can accurately predict the nonlinear characteristics normally found in FSI problems with complex geometries, moving boundaries, and large deformations. The instantaneous boundary velocity errors in the explicit BTDF scheme are well within $\mathcal{O}\left(h^2\right)$, which is aligned with the second-order approximation. Hence, these results demonstrate that the proposed explicit BTDF scheme can not only achieve similar accuracy to the implicit direct forcing scheme, but also comes at a much lower computational cost and memory requirements, allowing the proposed explicit BTDF scheme to be implemented for real-world FSI problems.

CRediT authorship contribution statement

Buchen Wu: Writing – review & editing, Writing – original draft, Visualization, Validation, Software, Methodology, Formal analysis, Data curation, Conceptualization. **HsuChew Lee:** Writing – review & editing, Writing – original draft. **Chang Shu:** Writing – review & editing, Writing – original draft, Supervision, Resources, Project administration, Formal analysis, Conceptualization. **Minping Wan:** Writing – review & editing, Writing – original draft, Supervision, Resources, Project administration, Funding acquisition, Formal analysis, Conceptualization.

Declaration of competing interest

The authors declare that they have no known competing financial interests or personal relationships that could have appeared to influence the work reported in this paper.

Data availability

The data of this study are available within the article.

Acknowledgments

This work has been supported by the Key-Area Research and Development Program of Guangdong Province, China (Grant No. 2021B01011 90003), the Department of Science and Technology of Guangdong Province, China (Grant No. 2020B1212030001), and the Shenzhen Science & Technology Program, China (Grant No. KQTD20180411143441009). Numerical simulations have been supported by the Center for Computational Science and Engineering of Southern University of Science and Technology, China.

References

[1] Dowell EH, Hall KC. Modeling of fluid-structure interaction. Annu Rev Fluid Mech 2001;33(1):445–90.

[2] Zhang Z, Liu M. A decoupled finite particle method for modeling incompressible flows with free surfaces. Appl Math Model 2018;60:606–33.

[3] Laima S, Wu B, Jiang C, Chen W, Li H. Numerical study on Reynolds number effects on the aerodynamic characteristics of a twin-box girder. Wind Struct 2019;28(5):285.

[4] Wu B, Laima S. Experimental study on characteristics of vortex-induced vibration of a twin-box girder and damping effects. J Fluids Struct 2021;103:103282.

[5] Zhang Z, Shu C, Liu Y, Liu W, Khalid MSU. An improved M-SPEM for modeling complex hydroelastic fluid-structure interaction problems. J Comput Phys 2023;488:112233.

[6] Mittal R, Iaccarino G. Immersed boundary methods. Annu Rev Fluid Mech 2005;37:239–61.

[7] Sotiropoulos F, Yang X. Immersed boundary methods for simulating fluid–structure interaction. Prog Aerosp Sci 2014;65:1–21.

[8] Huang W-X, Tian F-B. Recent trends and progress in the immersed boundary method. Proc Inst Mech Eng C 2019;233(23–24):7617–36.

[9] Sui Y, Chew Y-T, Roy P, Low H-T. A hybrid method to study flow-induced deformation of three-dimensional capsules. J Comput Phys 2008;227(12):6351–71.

[10] Huang W-X, Chang CB, Sung HJ. Three-dimensional simulation of elastic capsules in shear flow by the penalty immersed boundary method. J Comput Phys 2012;231(8):3340–64.

[11] Huang W-X, Sung HJ. An immersed boundary method for fluid–flexible structure interaction. Comput Methods Appl Mech Engrg 2009;198(33–36):2650–61.

[12] Wu B, Lu J, Lee H, Shu C, Wan M. An explicit immersed boundary-reconstructed thermal lattice Boltzmann flux solver for thermal–fluid-structure interaction problems. Int J Mech Sci 2022;235:107704.

[13] Wu B, Lu J, Lee H, Shu C, Wan M. An efficient explicit immersed boundary-reconstructed lattice Boltzmann flux solver for isothermal fluid-structure interaction problems with large deformations and complex geometries. Appl Math Model 2023;114:627–45.

[14] Wu B, Lu J, Lee H, Shu C, Wan M. An explicit boundary condition-enforced immersed boundary-reconstructed thermal lattice Boltzmann flux solver for thermal-fluid-structure interaction problems with heat flux boundary conditions. J Comput Phys 2023;485:112106.

[15] Wu B, Shu C, Wan M. An implicit immersed boundary method for robin boundary condition. Int J Mech Sci 2023;108694.

[16] Zhang D, Li Y, Zhang J, Yuan H, Zhang Z. Pore-scale numerical study: Brine water crystallization with ice crystal particle motion using the LBM-PFM-IBM. Appl Therm Eng 2023;234:121258.

[17] Kang L, Xiong S, Wu B, Li C, Ge M, Yuan D, et al. Force decomposition on flapping flexible plate via impulse theory and dynamic mode decomposition. Phys Fluids 2023;35(10).

[18] Borazjani I, Sotiropoulos F. Numerical investigation of the hydrodynamics of carangiform swimming in the transitional and inertial flow regimes. J Exp Biol 2008;211(10):1541–58.

[19] Borazjani I, Sotiropoulos F. On the role of form and kinematics on the hydrodynamics of self-propelled body/caudal fin swimming. J Exp Biol 2010;213(1):89–107.

[20] Dong H, Bozkurttas M, Mittal R, Madden P, Lauder G. Computational modelling and analysis of the hydrodynamics of a highly deformable fish pectoral fin. J Fluid Mech 2010;645:345–73.

[21] Wu B, Shu C, Lee H, Wan M. The effects of caudal fin's bending stiffness on a self-propelled carangiform swimmer. Phys Fluids 2022;34(4):041901.

[22] Wu B, Shu C, Lee HC, Wan M. Numerical study on the hydrodynamic performance of an unconstrained carangiform swimmer. Phys Fluids 2022;34(12):121902.

[23] Wu B, Shu C, Wan M, Wang Y, Chen S. Hydrodynamic performance of an unconstrained flapping swimmer with flexible fin: A numerical study. Phys Fluids 2022;34(1):011901.

[24] Yang L, Shu C, Yang W, Wang Y, Wu J. An immersed boundary-simplified sphere function-based gas kinetic scheme for simulation of 3D incompressible flows. Phys Fluids 2017;29(8):083605.

[25] Wang J, Ren Y, Li C, Dong H. Computational investigation of wing-body interaction and its lift enhancement effect in hummingbird forward flight. Bioinspir Biomimet 2019;14(4):046010.

[26] Huang Q, Bhat SS, Yeo EC, Young J, Lai JC, Tian F-B, et al. Power synchronisations determine the hovering flight efficiency of passively pitching flapping wings. J Fluid Mech 2023;974:A41.

[27] Ma J, Xu L, Tian F-B, Young J, Lai JC. Dynamic characteristics of a deformable capsule in a simple shear flow. Phys Rev E 2019;99(2):023101.

[28] Ma J, Huang Q, Zhu Y, Xu Y-Q, Tian F-B. Effects of fluid rheology on dynamics of a capsule through a microchannel constriction. Phys Fluids 2023;35(9).

[29] Zhang H, Liu Y, Zhang Z, Wang L-P, Shu C. An immersed boundary-lattice Boltzmann flux solver for simulation of flows around structures with large deformation. Phys Fluids 2023;35(3).

[30] Teixeira PRdF, Awruch AM. Numerical simulation of fluid–structure interaction using the finite element method. Comput & Fluids 2005;34(2):249–73.

[31] Hübner B, Walhorn E, Dinkler D. A monolithic approach to fluid–structure interaction using space–time finite elements. Comput Methods Appl Mech Engrg 2004;193(23–26):2087–104.

[32] Gerstenberger A, Wall WA. An extended finite element method/Lagrange multiplier based approach for fluid–structure interaction. Comput Methods Appl Mech Engrg 2008;197(19–20):1699–714.

[33] Hirt CW, Amsden AA, Cook J. An arbitrary Lagrangian-Eulerian computing method for all flow speeds. J Comput Phys 1974;14(3):227–53.

[34] Liu H, Kawachi K. A numerical study of undulatory swimming. J Comput Phys 1999;155(2):223–47.

[35] Udaykumar H, Mittal R, Rampunggoon P, Khanna A. A sharp interface cartesian grid method for simulating flows with complex moving boundaries. J Comput Phys 2001;174(1):345–80.

[36] Glowinski R, Pan T-W, Hesla TI, Joseph DD, Periaux J. A fictitious domain approach to the direct numerical simulation of incompressible viscous flow past moving rigid bodies: application to particulate flow. J Comput Phys 2001;169(2):363–426.

[37] Ramamurti R, Sandberg WC. A three-dimensional computational study of the aerodynamic mechanisms of insect flight. J Exp Biol 2002;205(10):1507–18.

[38] Peskin CS. Numerical analysis of blood flow in the heart. J Comput Phys 1977;25(3):220–52.

[39] Goldstein D, Handler R, Sirovich L. Modeling a no-slip flow boundary with an external force field. J Comput Phys 1993;105(2):354–66.

[40] Mohd-Yusof J. Combined immersed-boundary/b-spline methods for simulations of flow in complex geometries. Center Turbulence Res Ann Res Briefs 1997;161(1):317–27.

[41] Fadlun E, Verzicco R, Orlandi P, Mohd-Yusof J. Combined immersed-boundary finite-difference methods for three-dimensional complex flow simulations. J Comput Phys 2000;161(1):35–60.

[42] Uhlmann M. An immersed boundary method with direct forcing for the simulation of particulate flows. J Comput Phys 2005;209(2):448–76.

[43] Tenneti S, Garg R, Subramaniam S. Drag law for monodisperse gas–solid systems using particle-resolved direct numerical simulation of flow past fixed assemblies of spheres. Int J Multiphase Flow 2011;37(9):1072–92.

[44] Vanella M, Fitzgerald T, Preidikman S, Balaras E, Balachandran B. Influence of flexibility on the aerodynamic performance of a hovering wing. J Exp Biol 2009;212(1):95–105.

[45] Kidanemariam AG, Uhlmann M. Direct numerical simulation of pattern formation in subaqueous sediment. J Fluid Mech 2014;750:R2.

[46] Su S-W, Lai M-C, Lin C-A. An immersed boundary technique for simulating complex flows with rigid boundary. Comput & Fluids 2007;36(2):313–24.

[47] Luo K, Wang Z, Fan J, Cen K. Full-scale solutions to particle-laden flows: Multidirect forcing and immersed boundary method. Phys Rev E 2007;76(6):066709.

[48] Wang Z, Fan J, Luo K. Combined multi-direct forcing and immersed boundary method for simulating flows with moving particles. Int J Multiph Flow 2008;34(3):283–302.

[49] Kang SK, Hassan YA. A comparative study of direct-forcing immersed boundary-lattice Boltzmann methods for stationary complex boundaries. Internat J Numer Methods Fluids 2011;66(9):1132–58.

[50] Kempe T, Fröhlich J. An improved immersed boundary method with direct forcing for the simulation of particle laden flows. J Comput Phys 2012;231(9):3663–84.

[51] Delouei AA, Nazari M, Kayhani M, Succi S. Non-Newtonian unconfined flow and heat transfer over a heated cylinder using the direct-forcing immersed boundary–thermal lattice Boltzmann method. Phys Rev E 2014;89(5):053312.

[52] Favier J, Revell A, Pinelli A. A lattice Boltzmann–Immersed boundary method to simulate the fluid interaction with moving and slender flexible objects. J Comput Phys 2014;261:145–61.

[53] Li C, Wang L-P. An immersed boundary-discrete unified gas kinetic scheme for simulating natural convection involving curved surfaces. Int J Heat Mass Transfer 2018;126:1059–70.

[54] Pepona M, Favier J. A coupled immersed boundary–lattice Boltzmann method for incompressible flows through moving porous media. J Comput Phys 2016;321:1170–84.

[55] Jiang M, Liu Z. A boundary thickening-based direct forcing immersed boundary method for fully resolved simulation of particle-laden flows. J Comput Phys 2019;390:203–31.

[56] Park H, Pan X, Lee C, Choi J-I. A pre-conditioned implicit direct forcing based immersed boundary method for incompressible viscous flows. J Comput Phys 2016;314:774–99.

[57] Xu T, Choi J-I. Stable monolithic immersed boundary projection method for particle sedimentation with heat transfer at density ratios near unity. Phys Fluids 2023;35(10).

[58] Lu J, Lei H, Dai C, Yang L, Shu C. Analyses and reconstruction of the lattice Boltzmann flux solver. J Comput Phys 2022;110923.

[59] Yang X, Zhang X, Li Z, He G-W. A smoothing technique for discrete delta functions with application to immersed boundary method in moving boundary simulations. J Comput Phys 2009;228(20):7821–36.

[60] Luo K, Zhuang Z, Fan J, Haugen NEL. A ghost-cell immersed boundary method for simulations of heat transfer in compressible flows under different boundary conditions. Int J Heat Mass Transfer 2016;92:708–17.

[61] Örley F, Pasquariello V, Hickel S, Adams NA. Cut-element based immersed boundary method for moving geometries in compressible liquid flows with cavitation. J Comput Phys 2015;283:1–22.

[62] Liao C-C, Chang Y-W, Lin C-A, McDonough J. Simulating flows with moving rigid boundary using immersed-boundary method. Comput & Fluids 2010;39(1):152–67.

[63] Wang Y, Shu C, Yang L, Sun Y. On the immersed boundary-lattice Boltzmann simulations of incompressible flows with freely moving objects. Internat J Numer Methods Fluids 2017;83(4):331–50.

[64] Zhang Z, Walayat K, Chang J, Liu M. Meshfree modeling of a fluid-particle two-phase flow with an improved SPH method. Internat J Numer Methods Engrg 2018;116(8):530–69.

[65] Zhang Z, Walayat K, Huang C, Chang J, Liu M. A finite particle method with particle shifting technique for modeling particulate flows with thermal convection. Int J Heat Mass Transfer 2019;128:1245–62.

[66] Huang W-X, Sung HJ. Three-dimensional simulation of a flapping flag in a uniform flow. J Fluid Mech 2010;653:301.

[67] Ma J, Wang Z, Young J, Lai JC, Sui Y, Tian F-B. An immersed boundary-lattice Boltzmann method for fluid-structure interaction problems involving viscoelastic fluids and complex geometries. J Comput Phys 2020;415:109487.

[68] Lee I, Choi H. A discrete-forcing immersed boundary method for the fluid–structure interaction of an elastic slender body. J Comput Phys 2015;280:529–46.

[69] de Tullio MD, Pascazio G. A moving-least-squares immersed boundary method for simulating the fluid–structure interaction of elastic bodies with arbitrary thickness. J Comput Phys 2016;325:201–25.

[70] Tian F-B, Dai H, Luo H, Doyle JF, Rousseau B. Fluid–structure interaction involving large deformations: 3D simulations and applications to biological systems. J Comput Phys 2014;258:451–69.